Rare Metal Materials and Engineering
Volume **, Issue **, ***8 **
Available online at **www.rmme.ac.cn**

Science Press ARTICLE

Cite this article as: Rare Metal Materials and Engineering

DOI: https://doi.org/10.12442/j.issn.1002-185X.20260162

Optimization of Precision Hot Forging Process for High-Strength Aluminum Alloy Wheel Hubs Based on Simulation-Experiment Coupling

Guo Guixing [1], Huang Xiaomin[1, 2], Sun Fu [3], Wu Weiqi [3], Mao Qilin [3], Ji Hongchao[1, 2]

[1] College of Mechanical Engineering, North China University of Science and Technology, Tangshan 063210, China; [2] Yanzhao Iron and Steel Laboratory, North China University of Science and Technology, Tangshan 063210, China; [3] China MCC22 Group Corporation Ltd., Tangshan 063035, China

Abstract: In response to the susceptibility of conventional cast wheels to forming defects and the high demand for energy conservation and emission reduction in modern vehicles, a two-stage precision hot forging process was designed to fabricate high-strength and lightweight 7050 aluminum alloy wheels. The hot deformation characteristics of 7050 aluminum alloy billets were systematically examined through isothermal hot compression tests. Finite element models for the pre-forging and final-forging operations were developed via Deform-3D software to conduct full-process numerical simulations of the wheel hub hot forging process and analyze the distribution characteristics of various physical field variables. A mathematical regression model was constructed based on the response surface methodology. Aiming at the dual objectives of reducing forging load and minimizing forging damage, key process parameters including initial forging temperature, die forging speed, and friction coefficient were optimized. The optimization outcomes demonstrated that the peak loads in the pre-forging and final-forging stages were reduced by 22.46% and 13.26%, respectively. The maximum damage zone of the forging was significantly reduced, and the overall damage level was remarkably lowered. Forging experiments were performed under the optimal process parameters, and the forgings exhibited excellent forming quality with comprehensive properties meeting industrial technical requirements.

Key words: 7050 aluminum alloy; Wheel hub; Thermal deformation behavior; Numerical simulation; Response surface optimization

1 Introduction

As global carbon emission regulations continue to tighten and consumers increasingly demand better vehicle performance, lightweight design and energy efficiency have emerged as the primary driving forces behind innovation in the automotive sector[1,2]. Wheels, which serve as critical structural components responsible for bearing complex loads and transmitting torque, play a pivotal role in vehicle lightweighting. By reducing unsprung weight, lightweight wheels lower rolling resistance and energy consumption while improving vehicle handling stability, making them an indispensable approach to enhancing automobile energy efficiency[3,4]. However, wheels manufactured using traditional casting techniques often suffer from a range of defects, including coarse microstructures, shrinkage porosity, gas pores, and oxide inclusions. These deficiencies inevitably limit the service performance of cast wheels and prevent them from meeting the stringent lightweight requirements for high strength and

Received date:
Foundation item: Scientific Research Project of Colleges and Universities in Hebei Province (QN2025291); Project of Yanzhao Iron and Steel Laboratory (25361003D); Open Fund Project of National Key Laboratory of Material Forming and Die Technology, Huazhong University of Science and Technology (P2025-039)
Corresponding author: Ji Hongchao, Ph.D., Professor, College of Mechanical Engineering, North China University of Science and Technology, Tangshan 063210, P. R. China, Tel: 0086-315-8805446, E-mail: jihongchao@ncst.edu.cn

structural reliability. Unlike cast components, forging technologies can significantly improve both the dimensional accuracy and mechanical properties of formed parts[5-8]. In response to the growing demand for higher-quality wheel forgings, extensive research is currently underway on precision hot forging forming processes.

Precision hot forging is a manufacturing technique characterized by complex processes and relatively high costs. Before conducting actual forging trials, it is essential to analyze the forming process through finite element simulation to accelerate the R&D process and cut down experimental trial costs[9-11]. Qian et al.[12] employed finite element analysis to study the entire forming process of a large steel ring—from ingot to ring blank to rolled ring—analyzing strain evolution and distribution patterns alongside temperature, dynamic recrystallization, and grain size evolution characteristics. Chen et al.[13] achieved precise modeling of temperature detection and prediction during the forging of large S355NL ring forgings by integrating a backpropagation neural network algorithm with finite element numerical simulation. Deb et al.[14] explored the influences of forging passes and temperature on microstructural refinement in multi-axis forging through numerical simulation. Thus, an optimal processing scheme was determined, which effectively enhanced microstructural homogeneity and tensile properties, while retaining favorable ductility. Dong et al.[15] integrated finite element simulations with flat forging experiments to systematically investigate the effects of punch protrusion height, cup wall thickness, and initial sheet thickness on the forming quality of flanged cup-shaped components. They successfully fabricated qualified parts, which confirmed the practicality and reliability of the proposed forming process. Chamanfar et al.[16] utilized the Deform software to establish a finite element model for the hot forging of nickel-based superalloys. The simulated true stress–strain curves and average grain sizes exhibited excellent consistency with the corresponding experimental measurements.

In the course of forging operations, thermal processing parameters exert a notable impact on the forming quality of forged components[17-19]. Zhu et al.[20] developed a three-dimensional nonlinear transient thermo-mechanical coupling finite element model specifically for the multi-directional forging of Ti65 alloy. Through this model, they examined how processing parameters affect the alloy's mechanical behaviors, and further optimized the forging process to effectively mitigate the risk of cracking. Zhang et al.[21] utilized Deform software to establish a thermo-mechanical-strain coupling finite element model, with the aim of optimizing radial forging parameters. This optimization approach not only achieved uniform deformation and inhibited abnormal grain growth but also eliminated surface cracks during the forming of large pure tungsten rods, ultimately producing high-quality forged products. Kim et al.[22] combined finite element analysis with deep neural network models to optimize the forging process parameters of Ti-6242 alloy, successfully realizing grain refinement and avoiding the formation of forming defects. Deng et al.[23] carried out multi-objective optimization of the green manufacturing route for hot forging of Ti-6Al-4V alloy connecting rods, integrating orthogonal experiments with Deform-3D numerical simulations. The optimal processing parameters were identified through visualization analysis, range analysis, and comprehensive frequency analysis. Łukaszek-sołek et al.[24] determined the optimal thermomechanical processing parameters for 4340 steel forging by establishing a correlation between processing maps and microstructural variations. Obiko et al.[25] implemented multi-objective optimization of forging temperature, die lifting speed, die temperature, and friction coefficient, leveraging the Deform 3D simulation platform in combination with the Taguchi method. Huang et al.[26] integrated finite element numerical simulation with the response surface method to accomplish multi-objective optimization of the hot forging process for a coupling gear combination blank, resulting in forged products with excellent strength and toughness.

In light of the geometric configuration of the wheel hub forging and the process features of aluminum alloy forging, a two-stage forming scheme composed of pre-forging and final forging is put forward to realize the high-performance forming of 7050 aluminum alloy wheel hubs. A comprehensive exploration is implemented by integrating theoretical analysis, numerical simulation and pilot forging trials. Isothermal hot compression experiments are conducted to develop the high-temperature constitutive model of the forging blank, and the optimal hot deformation interval of the alloy is determined with the aid of processing maps. The deformation behaviors during forging and the evolutionary characteristics of major field variables are studied using Deform simulation software. Response surface methodology is employed to reveal the interactive coupling mechanisms of different forging parameters, with the aim of optimizing and locking in the best parameter combination for the process. Finally, the forming quality is evaluated by means of trial production tests, which validates the feasibility of the forging process parameters and provides a theoretical foundation and technical support for actual production.

2 Materials and Experimental Procedures

2.1 Isothermal hot compression tests

Aluminum alloy 7050 is an ideal lightweight, high-strength material. Thanks to its combination of high strength, good toughness, and lightweight characteristics, it has become the material of choice in fields with stringent requirements for material performance and weight reduction, such as aerospace and high-end equipment[27–29]. 7050 aluminum alloy was adopted as the material for the wheel hub forging, whose chemical composition is listed in Table 1.

Table 1 Chemical composition of 7050 aluminum alloy (%, mass fraction)

Elements	Si	Fe	Cu	Mn	Mg	Cr	Zn	Ti	Zr	Al
Content	0.12	0.15	2.0-2.6	0.10	1.9-2.6	0.04	5.7-6.7	0.06	0.08-0.15	Balance

As a typical wrought aluminum alloy, 7050 aluminum alloy is usually formed by hot forging. To accurately investigate its metal flow behavior during high-temperature forging, isothermal hot compression tests are conducted[30]. A Gleeble-3800 thermo-mechanical simulator was used to simulate the hot deformation behavior of metallic materials. Small cylindrical specimens with a size of Φ8 mm×12 mm were cut from the billet by wire electrical discharge machining, and both ends were polished to be smooth. To reduce the influence of friction on the experimental data and ensure the uniformity of specimen deformation, graphite sheets were applied for lubrication at the contact surface between the specimen and the indenter. The specimen was heated to the target temperature at a heating rate of 3 °C/s and held for 180 s to ensure uniform temperature distribution inside the specimen, followed by a compression test with a deformation amount of 50% (corresponding to a true strain of approximately 0.69). Immediately after deformation, water quenching was performed to retain the high-temperature deformed microstructure. The hot compression test apparatus and process route diagram are illustrated in Figure 1.

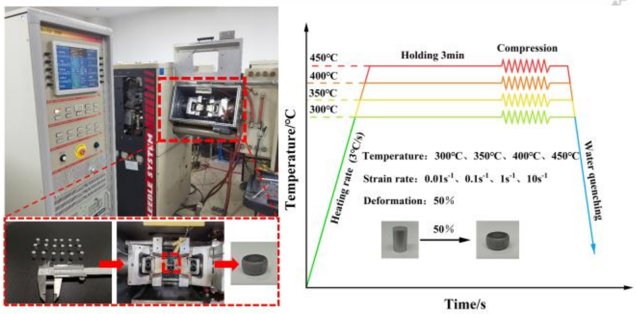

Fig.1 Experimental apparatus and process route diagram

Isothermal hot compression tests were conducted under four temperatures (300, 350, 400, and 450 °C) and four strain rates (0.01, 0.1, 1, and 10 s^{-1}), resulting in a total of 16 experimental conditions. According to the experimental data under various deformation parameters, the corresponding stress-strain curves are plotted using Origin software, as shown in Figure 2.

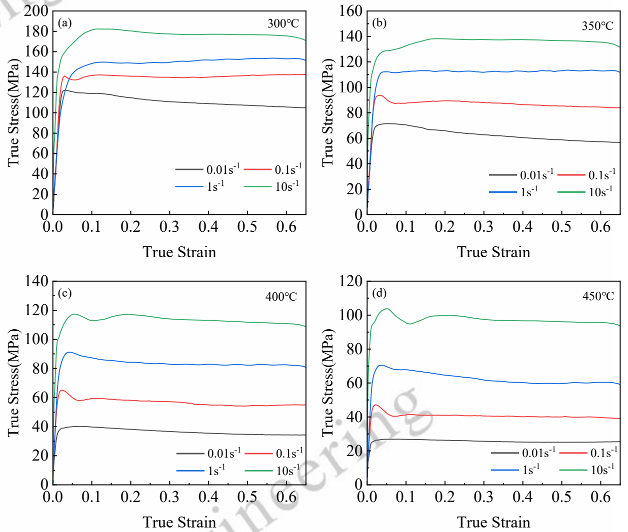

Fig.2 Stress-strain curves of 7050 aluminum alloy under different deformation conditions: (a) 300℃, (b) 350℃, (c) 400℃, (d)450℃

2.2 Development of constitutive models

Drawing upon the experimentally collected data, a constitutive model is constructed to characterize the coupling correlation between flow stress, strain rate, and deformation temperature throughout hot deformation. The classical Arrhenius hyperbolic sine model is utilized to construct the constitutive relationship, whose specific expression is given in Equation (1):

$$\dot{\varepsilon}=\begin{cases} A\sigma^{m}\exp(\frac{-Q}{RT}), & \alpha\sigma<0.8 \\ A\exp(\beta\sigma)\exp(\frac{-Q}{RT}), & \alpha\sigma>1.2 \\ A[\sinh(\alpha\sigma)]^{n}\exp(\frac{-Q}{RT}), & \text{for all } \sigma \end{cases} \tag{1}$$

In the formula:

ε — Strain rate, s^{-1};

σ — Flow stress, MPa;

Q — Activation energy for hot deformation, J/mol;

R — Molar gas constant, 8.314J/(mol·k);

T — Absolute temperature, K;

A, n, m, α, β—Material constants, where α=β/m.

During thermal deformation, flow stress varies with strain evolution. To further enhance the prediction precision of the Arrhenius constitutive model, a strain-compensated mechanism is introduced to establish the strain-compensated constitutive equation. Within the true strain range of 0–0.69, flow stress values are extracted at an interval of 0.05. The four material parameters (α, n, Q and lnA) under various true strains are computed separately. The polynomial fitting approach is utilized to construct the correlative model between the material parameters and strain, as presented in Equation (2). After verification of fitting accuracy through multiple trials, a 7th-order polynomial is finally determined for parameter fitting.

$$\begin{cases} \alpha = \alpha_0 + \alpha_1\varepsilon + \alpha_2\varepsilon^2 + \alpha_3\varepsilon^3 + \alpha_4\varepsilon^4 + \alpha_5\varepsilon^5 + \alpha_6\varepsilon^6 + \alpha_7\varepsilon^7 \\ n = n_0 + n_1\varepsilon + n_2\varepsilon^2 + n_3\varepsilon^3 + n_4\varepsilon^4 + n_5\varepsilon^5 + n_6\varepsilon^6 + n_7\varepsilon^7 \\ Q = Q_0 + Q_1\varepsilon + Q_2\varepsilon^2 + Q_3\varepsilon^3 + Q_4\varepsilon^4 + Q_5\varepsilon^5 + Q_6\varepsilon^6 + Q_7\varepsilon^7 \\ \ln A = A_0 + A_1\varepsilon + A_2\varepsilon^2 + A_3\varepsilon^3 + A_4\varepsilon^4 + A_5\varepsilon^5 + A_6\varepsilon^6 + A_7\varepsilon^7 \end{cases} \quad (2)$$

The polynomial fitting curves of each material parameter are depicted in Figure 3, while the relevant polynomial coefficients are tabulated in Table 2. As observed in the figure, the calculated discrete points of each material parameter are in good agreement with the fitting curves, indicating that the polynomial relationship between the parameters and strain has a high correlation.

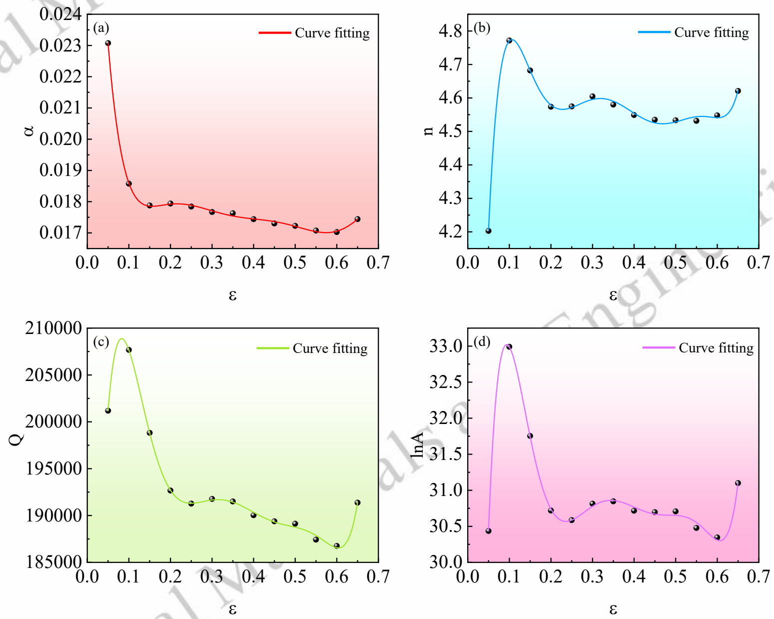

Fig.3 Correlation plot of fitted parameters: (a) α − ε, (b) n − ε, (c), Q – ε, (d) lnA − ε

Table 2 Fitting Equations for Material Parameters of 7050 Aluminum Alloy

Fitting coefficient	α	Fitting coefficient	n	Fitting coefficient	Q（J/mol）	Fitting coefficient	lnA
α_0	0.03801	n_0	1.24723	Q_0	126801.1512	A_0	12.83048
α_1	-0.47687	n_1	103.20263	Q_1	2793880.72	A_1	634.83486
α_2	4.54337	n_2	-1160.61471	Q_2	-3.49E+07	A_2	-7489.13694
α_3	-22.57519	n_3	6502.4519	Q_3	2.05058E8	A_3	42848.39538
α_4	63.45396	n_4	-20129.9332	Q_4	-6.54E+08	A_4	-134345.855
α_5	-101.6221	n_5	34999.39814	Q_5	1.16499E9	A_5	236366.5115
α_6	86.33488	n_6	-32022.9047	Q_6	-1.09E+09	A_6	-219226.991
α_7	-30.14061	n_7	12003.12546	Q_7	4.18751E8	A_7	83484.4759

The strain-compensated Arrhenius constitutive model provides accurate prediction for the flow stress of the alloy throughout the entire deformation process, thus effectively extending the applicable range of the model. The specific constitutive relationship is expressed as follows.

$$\sigma = \frac{1}{\alpha}\ln\left\{\left(\frac{Z}{A}\right)^{\frac{1}{n}} + \left[\left(\frac{Z}{A}\right)^{\frac{2}{n}} + 1\right]^{\frac{1}{2}}\right\} \quad (3)$$

To assess the forecasting accuracy of the constructed constitutive model, the forecasted data from the model under diverse deformation conditions are compared with the experimental measurements. As observed in Figure 4, although slight fluctuations exist between the calculated values and the measured data, the changing tendency of flow stress computed by the model with true strain shows strong consistency with the experimental findings, and the overall deviation is relatively small. The results presented in this work demonstrate that the strain-compensated Arrhenius constitutive model established herein exhibits strong predictive performance, and is capable of accurately estimating the flow stress behavior of the alloy across a range of deformation conditions.

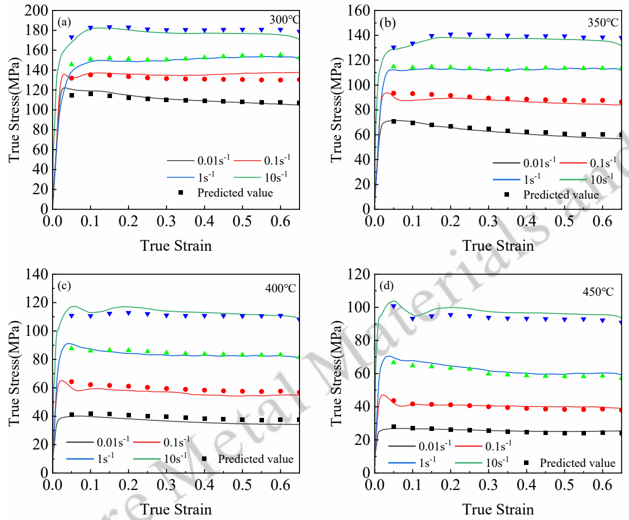

Fig.4 Assessment of predicted values against experimental results: (a)300℃, (b) 350℃, (c) 400℃, (d)450℃.

In order to quantitatively evaluate the prediction capability of the strain-compensated Arrhenius model developed in this work, we adopt two essential statistical metrics: the correlation coefficient R and the average absolute relative error (AARE, %). Figure 5 presents a detailed comparison of the consistency between the predicted flow stress values and the experimental measurements. The mathematical formulas for these two metrics are provided as follows:

$$AARE = \frac{1}{N}\sum_{i=1}^{N}\left|\frac{\sigma_{Ei}-\sigma_{Pi}}{\sigma_{Ei}}\right| \tag{4}$$

$$R = \frac{\sum_{i=1}^{N}\left(\sigma_{Ei}-\overline{\sigma_E}\right)\left(\sigma_{Pi}-\overline{\sigma_{Pi}}\right)}{\sqrt{\sum_{i=1}^{N}\left(\sigma_{Ei}-\overline{\sigma_E}\right)^2\sum_{i=1}^{N}\left(\sigma_{Pi}-\overline{\sigma_{Pi}}\right)^2}} \tag{5}$$

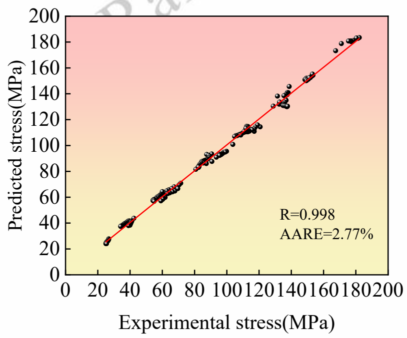

Fig.5 Correlation analysis of measured and predicted flow stress.

2.3 Construction of processing maps for aluminum alloy

In the present work, the processing map is constructed based on the dynamic material model (DMM), integrated with the isothermal hot compression experimental data of 7050 aluminum alloy for the wheel hub forging. The developed map is employed to assess the hot workability of 7050 aluminum alloy under a wide range of deformation temperatures and strain rates, investigate its deformation behaviors during hot plastic forming, and further identify the optimal hot processing window. The processing map is generated by overlaying the power dissipation diagram and the flow instability diagram. The underlying physical mechanism can be elaborated as follows: the total input energy P per unit volume of the alloy during hot plastic deformation consists of two components, namely the dissipative term G consumed by plastic deformation and the dissipative co-content J that drives microstructural evolution processes such as dynamic recrystallization and grain growth. Collectively, these parameters characterize the energy dissipation behavior of the alloy during hot deformation, as shown in Equation (6):

$$P = \sigma\dot{\varepsilon} = G + J = \int_0^{\dot{\varepsilon}}\sigma d\dot{\varepsilon} + \int_0^{\sigma}\dot{\varepsilon}d\sigma \tag{6}$$

The strain rate sensitivity index m determines the relationship between the energy dissipation term G and the dissipative co-content J. This parameter serves as a direct measure of the energy partitioning mechanism, and its corresponding mathematical expression is given below:

$$m = \frac{dJ}{dG} = \frac{\dot{\varepsilon}d\sigma}{\sigma d\dot{\varepsilon}} = \frac{d\ln\sigma}{d\ln\dot{\varepsilon}} \tag{7}$$

It can be derived from Equation (7) that the dissipative co-content J achieves its peak at m = 1, which represents an ideal linear dissipation state for the material during hot deformation. To describe the relationship between the actual dissipative co-content and its maximum possible value, the dissipation efficiency factor is introduced as follows:

$$\eta = \frac{J}{J_{\max}} = 2\left(1-\frac{1}{1+m}\right) = \frac{2m}{1+m} \tag{8}$$

Although the power dissipation map allows assessment of the microstructural softening mechanism degree in the alloy under different deformation conditions based on the η value, it cannot predict the flow instability characteristics during hot deformation. When developing the hot processing map for 7050 aluminum alloy, both the energy dissipation characteristics and the flow instability tendency of the alloy during hot deformation must be considered. The Prasad instability criterion is a widely accepted criterion for evaluating the flow instability characteristics of metallic materials during hot working, and its corresponding mathematical expression is given in Equation (9):

$$\xi(\dot{\varepsilon}) = \frac{\partial\ln\left[m/(m+1)\right]}{\partial\ln\dot{\varepsilon}} + m < 0 \tag{9}$$

To summarize, the higher the dissipation efficiency value, the larger the proportion of the dissipative co-content J in the overall energy dissipation P; this signifies that more energy is utilized to drive microstructural development, including dynamic recrystallization and dynamic recovery. This generally indicates that the softening mechanism during hot deformation is more sufficient, and the material has better hot workability. The instability criterion value varies with processing parameters. When the instability criterion value is negative, the corresponding region is the hot deformation instability zone. When the material is plastically deformed under these parameters, instability phenomena such as flow localization and adiabatic shear bands are very likely to occur. Therefore, this region should be excluded from the processing window.

The processing maps corresponding to true strains of 0.2, 0.4 and 0.6 are illustrated in Figure 6. Areas with elevated η values are marked in green, and flow instability zones are marked in red. Overall, with increasing strain, the power dissipation factor η in the suitable processing zone increases and the zone gradually expands, indicating better deformation stability within the appropriate parameter range at larger strains. The instability zones are mainly concentrated at low temperatures with both low and high strain rates. This is attributed to insufficient dynamic softening and low energy dissipation efficiency at low temperatures. As the true strain increases, the instability zones expand toward the medium-temperature region. The domains for safe processing predominantly lie within the high-temperature and low-strain-rate regions. With the aim of improving the hot deformation capacity of 7050 aluminum alloy, the favorable processing domain is tentatively identified based on the processing maps corresponding to various strain magnitudes: a deformation temperature range of 400–450 °C and a strain rate range of 0.01–0.1 s^{-1}.

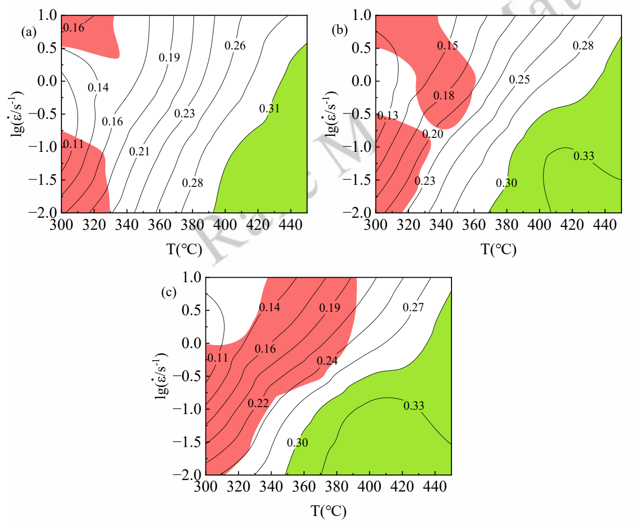

Fig.6 Processing maps at various true strains: (a) ε =0.2, (b) ε =0.4, (c) ε =0.6s

3 Finite Element Model Development and Results Analysis

3.1 Finite element model development

To ensure complete metal filling in the hub ribs and the circumferential zone of the wheel rim, a two-stage forming process combining pre-forging and final forging is adopted, taking into account factors such as forging forming accuracy and metal flow behavior. The schematic diagram of the wheel hub forging is shown in Fig. 7.

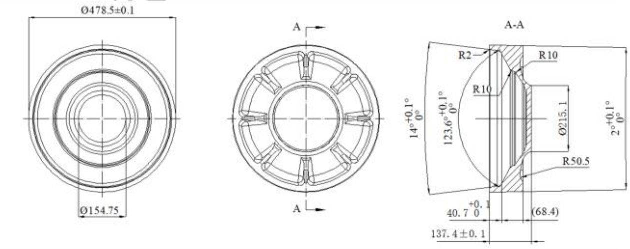

Fig.7 Schematic diagram of the wheel hub forging

The forming process flow is illustrated in Figure 8. Pre-forging is employed to preliminarily shape the blank into an intermediate form close to the final forging geometry, which reasonably distributes the metal volume in each section, optimizes the metal flow lines, and reduces the final forging load. Final forging is used to obtain the final shape and dimensions of the forging, ensuring clear contours, qualified dimensional accuracy and favorable surface quality, thus reducing the amount of subsequent machining.

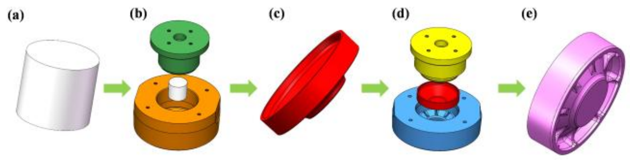

Fig.8 Process flow for the forging of aluminum alloy wheels: (a)billet, (b)pre-forging, (c)pre-forged component, (d)final forging, (e)final-forged component

To improve the reliability of finite element simulation, this study established a constitutive model of 7050 aluminum alloy based on isothermal hot compression tests for subsequent forming simulation. In the numerical simulation of large forgings, by customizing and adding 7050 aluminum alloy material in Deform-3D and setting reasonable boundary conditions, the temperature field evolution and deformation heating effect of parts with different sizes are considered, thus reducing the deviation introduced by the size difference between the specimen and the forging to a certain extent. The geometric model built in SolidWorks is properly simplified, exported as an STL file, and then converted into a finite element analysis model in Deform-3D, which provides a reliable model basis for the subsequent field-variable finite element simulation of the wheel hub hot forging process. The corresponding models for the wheel hub's pre-forging and final-forging operations are depicted in Figure 9.

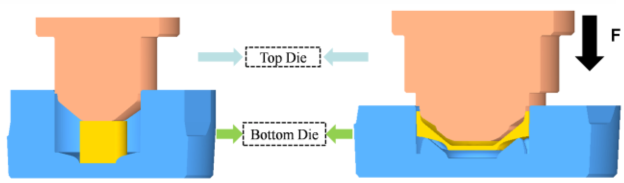

Fig.9 Finite element simulation models for pre-forging and final forging

Utilizing the optimal process parameters from the prior hot deformation behavior investigation, and accounting for the practical hot forging process features, the finite element model processing parameters are defined. The main settings cover model creation, tool definition, and boundary conditions, as summarized in Table 3. Increasing mesh density can improve the calculation accuracy in severely deformed areas, but will significantly increase the computational cost. Taking both computational efficiency and simulation accuracy into consideration, a finite element model with approximately 160,000 elements is established. During the simulation, remeshing is performed according to the mesh distortion, and FEM + meshing is adopted as the volume compensation method for forgings, to avoid mesh volume loss caused by large deformation and ensure the stability and accuracy of the calculation process.

Table 3 Parameter settings for numerical simulation of aluminum alloy wheel forming

Parameters	Numerical value
Number of billet cells	160000
Number of die cells	100000
Initial forging temperature of workpiece / (°C)	420
Die preheating temperature / (°C)	400
Interfacial heat transfer coefficient / (N·(s·mm·°C)⁻¹)	11
Heat transfer coefficient / (N·(s·mm·°C)⁻¹)	0.02
Friction coefficient	0.2
Thermal conductivity: 7050 Al alloy / (W/(m·K))	180.181

3.2 Analysis of numerical simulation findings

As depicted in Figure 10, the numerically simulated distributions of temperature, stress, and damage evolution throughout the wheel hub forging process are presented. As observed in Figure 10(a), the temperature in the central zone is relatively low. Plastic deformation within the annular forging tends to localize mainly in the spoke region, where the plastic heat converted from plastic working serves as the dominant cause of temperature elevation. Owing to the more intense deformation occurring in the spoke area, a greater amount of plastic heat is generated and retained, whereas the top section of the rim displays the lowest temperature as a result of sustained heat transfer to the die. According to Figure 10(b), the intermediate layer is subjected to greater mechanical constraint from the die during deformation, leading to an overall higher stress level. The central region undergoes only slight deformation with weak constraint, thus corresponding to lower stress values. Meanwhile, the upper rim region, where deformation is nearly finished and die constraint is gradually relieved, exhibits a noticeable reduction in stress. Figure 10(c) indicates that damage accumulates gradually from the center toward the outer edge, with damage values in the outer layer increasing continuously and reaching a maximum at the outermost boundary. Within the forged wheel hub, regions prone to damage are mainly distributed in the rim zone. This region exhibits relatively high overall stress levels, and the maximum damage zone overlaps with the lowest temperature zone. Forging damage will severely affect the forging quality.

Based on the Normalized Cockcroft & Latham damage model, as expressed in Eq. (10). The damage evolution trend during the forging forming process is predicted. The higher the damage accumulation value, the greater the risk of fracture in this area. In the subsequent forming experiments, the easily damaged areas will be inspected and verified.

$$C_d = \int_0^{\bar{\varepsilon}_f} \frac{\sigma^*}{\bar{\sigma}} d\bar{\varepsilon} \tag{10}$$

Where: C_d is the damage value; $\bar{\varepsilon}_f$ is the equivalent plastic strain at fracture; $\bar{\sigma}$ is the equivalent stress; σ^* is the maximum principal stress; $d\bar{\varepsilon}$ is the increment of equivalent plastic strain.

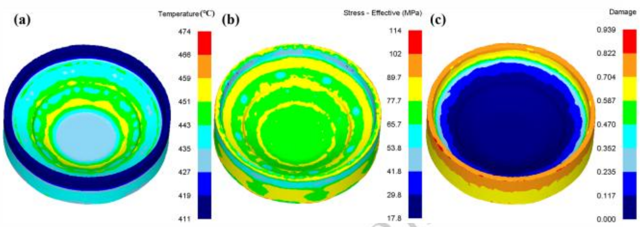

Fig.10 Numerical simulation results for the wheel hub forging: (a)temperature, (b)equivalent stress, (c)damage

Figure 11 presents the stroke-load curves corresponding to the top and bottom dies. The top die exerts a downward forging force, causing the billet to undergo plastic flow. As the material's deformation resistance needs to be surmounted, the load acting on the top die increases rapidly. As a supporting structure, the lower die bears the reverse reaction force transmitted by the deformed billet, thus presenting a negative load. The forging loads of the upper and lower dies are basically symmetrically distributed. Compared with final forging, pre-forging features a larger reduction and a higher deformation degree, resulting in a significantly higher forging load. Pre-forging therefore further reduces the load in the final forging stage. Excessively high forging loads can severely shorten the fatigue life of the primary load-bearing elements of the forging press, leading to degraded motion accuracy, impaired dimensional accuracy of the forging, and compromised forging quality. Excessively high loads also aggravate plastic deformation on the die cavity surface and accelerate die failure.

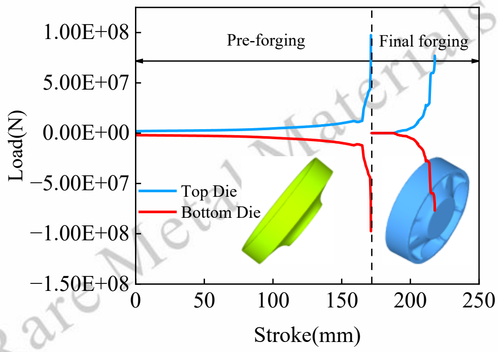

Fig.11 Stroke-load curve for upper and lower dies in wheel hub forging

Evaluation of the above numerical simulation outcomes demonstrates that excessive damage values and forging loads in the wheel hub forging process have a direct influence on the quality of the forged component. Accordingly, it is highly significant for the forging of 7050 aluminum alloy wheel hubs to appropriately optimize the forging process parameters and establish the optimal hot forging process parameters.

4 Parametric Optimization of Hot Forging

4.1 Establishing design variables and optimization targets

The rim area of the wheel hub forging is prone to severe damage and even cracking, which introduces potential safety hazards. As the wheel hub is critical to vehicle safety, performance and efficiency, high requirements are imposed on its forming quality. The load applied to the die directly affects its service life as well as the forming quality of the forging. In an effort to lower production costs and improve forming efficiency, the optimization of key process parameters is essential. According to the analytical results of processing maps, suitable initial forging temperature and deformation velocity exert a considerable influence on the final forging quality. Initial forging temperature, die forging velocity, and die-workpiece interfacial friction coefficient are designated as the input design variables, with forging damage index and die forging force established as the optimization targets.

4.2 Box-Behnken design of experiments

Using the Box–Behnken design in Design-Expert software, the experimental scheme is designed for various process parameters. The specific experimental parameters along with their corresponding designed levels are summarized in Table 4.

Table 4 Table of experimental factors and levels

Factors	Levels		
	-1	0	1
T (initial forging temperature, °C)	400	425	450
V (die forging speed, mm/s)	5	13	21
M (friction coefficient)	0.1	0.2	0.3

The experimental combinations are randomized in sequence, and coupled with the optimal processing range derived from the processing maps, a total of 17 experimental runs are designed. Simulation analyses for these distinct test schemes are conducted via Deform-3D software, and the simulation outcomes are presented in Table 5.

Table 5 Box-Behnken simulation test table

Number	T/(°C)	V/（mm/s）	M	Damage
1	400	13	0.1	0.955
2	425	21	0.1	0.97
3	425	5	0.1	0.912
4	425	13	0.2	0.94
5	425	13	0.2	0.932
6	400	13	0.3	0.963
7	450	5	0.2	0.85
8	425	13	0.2	0.931
9	425	13	0.2	0.934
10	425	21	0.3	0.927
11	425	13	0.2	0.945
12	450	13	0.3	0.838
13	425	5	0.3	0.838
14	400	5	0.2	0.89
15	450	21	0.2	0.862
16	400	21	0.2	0.984
17	450	13	0.1	0.945

4.3 Development of a response surface model

Utilizing the aforementioned dataset of 17 experimental trials, the corresponding response surface models for forging damage D and die forging load F are constructed, as depicted in Equations (11) and (12).

$$D = 0.9364 - 0.0371A + 0.0316B - 0.027C - 0.0205AB - 0.0288AC + 0.0078BC - 0.0132A^2 - 0.0267B^2 + 0.0021C^2 \quad (11)$$

$$F = 85.12 - 9.64A + 7.79B + 8.28C - 6.65AB - 2.58AC - 0.375BC + 4.04A^2 - 2.46B^2 + 0.715C^2 \quad (12)$$

In this equation: A represents the initial forging temperature of the workpiece (°C); B represents the die forging speed ($mm\cdot s^{-1}$); and C represents the coefficient of friction.

Analysis of variance was performed on the two constructed response surface models respectively. The results show that the P-values of both models are less than 0.0001, indicating that both models are highly significant. The P-values of the lack-of-fit term are 0.1437 and 0.1500 respectively, both greater than 0.05, indicating that there is no significant lack-of-fit in the models. The Adeq Precision values are 24.0756 and 26.4561, respectively, both greater than 14, demonstrating good fitting performance and a signal-to-noise ratio that meets the requirements. The relationship between the model-predicted outputs and the experimentally measured data is illustrated in Figure 12. For the developed response surface model, the coefficient of determination R^2 serves as a key metric to evaluate the goodness of fit. The R^2values corresponding to the two models are 0.986 and 0.9845, respectively, both close to 1, indicating high model accuracy. According to the ANOVA table and the predictive correlation, the developed second-order response surface models can effectively elucidate the variation trends of damage value and forging load as functions of process parameters. The optimization of process parameters based on these models can obtain high-precision optimization results.

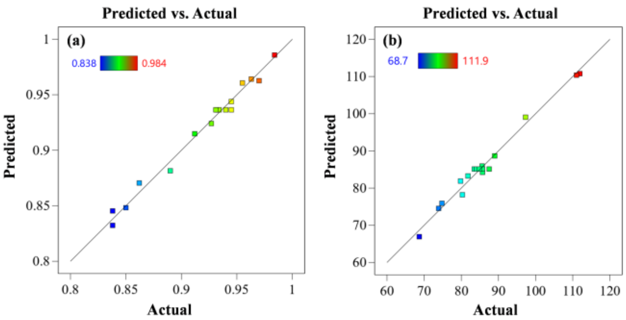

Fig.12 Prediction relationship of response surface models: (a)forging damage; (b)forging load

4.4 Response surface analysis and determination of optimal process parameters

Figures 13(a)–(c) respectively display the response surface relationships between the die forging load of the wheel hub forging, forging temperature and deformation speed under friction coefficients of 0.1, 0.2 and 0.3. At the same deformation temperature or forging speed, the die forging load shows an overall increasing trend as the friction coefficient rises. Elevated friction between the die and the forging elevates the resistance to metal flow, thus increasing the necessary load. At any friction coefficient, increasing the forging temperature reduces the die forging load. This is because a higher temperature enhances the plasticity of the hub material and decreases its deformation resistance, thus lowering the required forging load. At any friction coefficient, increasing the forging speed raises the deformation resistance of the material, leading to a significant rise in die forging load. The variation trend of die forging load with process parameters indicates that the coefficient of friction and temperature have the greatest influence on die forging load, while the effect of forging speed is relatively small.

Figures 13(d), (e), and (f) show the response surfaces of damage in wheel hub forgings as a function of the friction coefficient and forging temperature at forging speeds of 5 mm/s, 13 mm/s, and 21 mm/s, respectively. Under identical friction coefficient and temperature conditions, higher forging velocities tend to aggravate material damage. This can be attributed to the fact that elevated forging speeds enhance the inhomogeneity of plastic deformation, which in turn gives rise to more significant local stress concentrations and consequently more severe damage evolution. At any given forging speed, forging damage reduces as the forging temperature rises. Higher temperatures enhance the plasticity of the hub material; improved metal fluidity leads to a more uniform deformation process, reducing local stress concentrations and consequently lowering the degree of damage. At any given forging speed, an increase in the friction coefficient moderately mitigates damage in the rim region. This is because the heat generated by friction locally improves the surface temperature of the forging; the resulting temperature rise significantly enhances the fluidity of the surface metal, thereby preventing excessive damage in the rim edge regions. As shown in Figure 13, forging speed exerts the most significant effect on forging damage, followed by forging temperature and the friction coefficient.

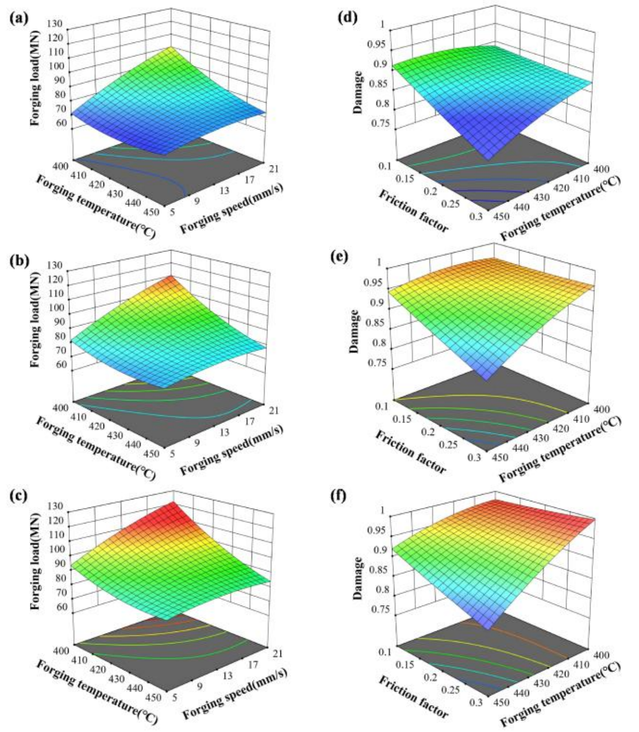

Fig.13 Response surface of forging loads and forging damage in aluminum alloy wheels as a function of preheating temperature, die-forging speed, and friction coefficient

Based on the results of the response surface optimization and in conjunction with actual production conditions, corresponding weights are assigned to each optimization objective. Forging load magnitude governs the tonnage of the equipment to be employed; if the load is too high, existing equipment fails to meet forming requirements. High loads also accelerate die wear, shortening die service life, and have a particularly significant impact on production efficiency and costs. Therefore, a weighting scheme of 5 for die forging load and 3 for forging damage is adopted to derive the optimal values of each process parameter. The resulting optimal process parameters are: forging temperature 450 °C, forging speed 5 mm/s, and coefficient of friction 0.216.

For a forging speed of 5 mm/s and a billet height of 187.5 mm, theoretical estimation based on the definition of strain rate shows that the initial strain rate of deformation is 0.027 s^{-1}. Furthermore, as illustrated in Figure 14, the distribution histogram of effective strain rate reveals that the strain rate under this working condition remains within the experimental range of 0.01-10 s^{-1}, which verifies that the parameters adopted in the hot compression test can effectively cover the deformation conditions of the actual forging process. As indicated by the effective strain rate distribution histogram, it can be seen that the strain rate in most areas of the forging during forming is 0.01-0.1s^{-1}, which is within the favorable processing window; the remaining areas are mainly in the medium strain rate range. According to the hot processing map, the optimized process parameter combination mainly falls within the safe processing zone with high power dissipation efficiency, and is far away from the instability zone characterized by adiabatic shear and localized flow.

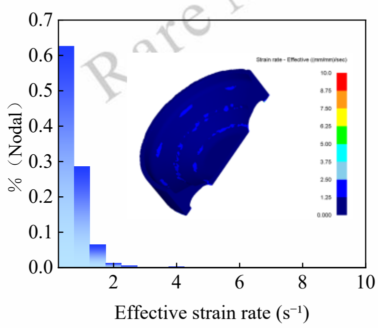

Fig.14 Distribution histogram of effective strain rate

5 Analysis and Discussion on Simulation Experimental Results

5.1 Analysis of the forging process

Numerical simulations are performed using the optimized process parameters derived from response surface methodology to analyze the relevant field variables throughout the wheel hub forming process. Figures 15(a) and (b) illustrate the pre-forging stage of the wheel hub forging, with Figures 15(c) and (d) depicting the final forging stage. During the pre-forging stage, the pre-shaped blank is forced into the pre-forging die cavity. The material flows in the direction perpendicular to the die cavity, causing the bowl-shaped side walls to be thinned and the boss to be compacted, resulting in a transition blank. In the final forging process, the material flows into the wheel spoke cavities, completing the filling of the spoke details and the overall filling of the wheel hub.

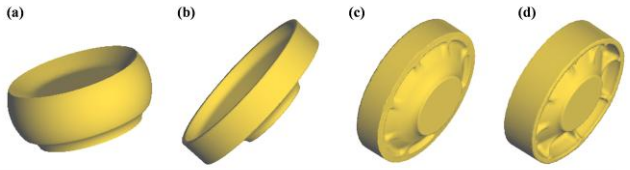

Fig.15 Wheel hub forging process: (a) upsetting stage, (b)pre-forging stage, (c)cavity filling stage, (d)final forging stage

The forming quality of a forged component relies, on the one hand, on the fullness of its macroscopic contour and, on the other hand, on the distribution of internal metal flow lines. Figures 16(a) and (b) and Figures 16(c) and (d) show the internal metal flow lines of the forging during pre-forging and final forging, respectively. During the pre-forging process, the flow lines exhibit a uniform, parallel, and continuous distribution, aligned with the primary deformation direction of the pre-forging. The flow lines begin to extend toward the initial structure of the forging, exhibiting a gentle, directed turn, yet remain continuous overall. During the final forging process, the flow lines completely conform to the geometric contour of the final forging, and the flow lines in the detailed transition zones are continuous without interruption. Considering the metal flow lines throughout the entire forging process from pre-forging to final forging, the flow lines maintain good continuity and a reasonable spatial distribution; no forming defects such as eddy currents, interlacing, convection, folding, or fractures are observed in the flow lines.

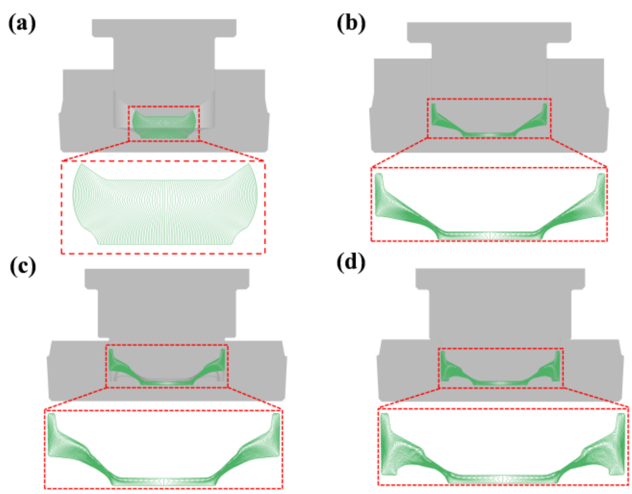

Fig.16 Metal flow line distribution in wheel hub forging: (a) upsetting stage, (b)pre-forging stage, (c)cavity filling stage, (d)final

forging stage

5.2 Analysis of the forging temperature field

Figure 17 depicts the temperature distribution of the billet during the entire hot forging process. The temperature distribution of the pre-forged part is generally uniform and gradual: temperatures are concentrated in the range of 420–438°C, with only slight fluctuations in the edge regions and no obvious local high- or low-temperature zones. This uniform temperature distribution ensures uniform deformation of the material during the pre-forging stage. The temperature distribution of the final forging exhibits regional variations, with localized high-temperature zones appearing in detailed forming areas such as the spokes and low-temperature zones along the upper edges of the rim. The temperature gradient is significantly greater than in the pre-forging stage. Plastic deformation is more concentrated in detailed areas such as the spokes, resulting in a significant increase in heat generated by deformation; the rim region features a larger contact area with the final forging die cavity, along with tighter contact and longer contact time, which allows for rapid heat dissipation in the contact zones. The temperature trends are consistent with those observed during the actual forging process.

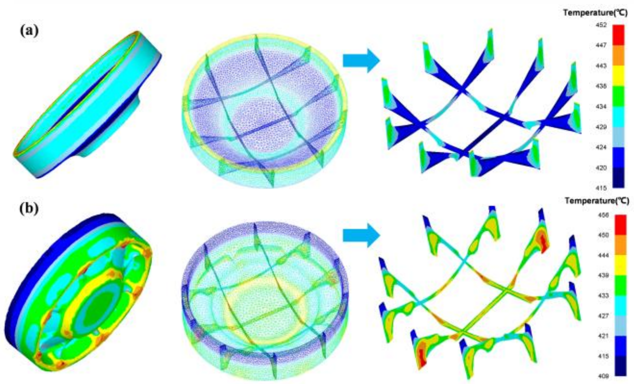

Fig.17 Temperature distribution diagram and cross-sectional views during the forging process: (a)pre-forging, (b)final forging

5.3 Analysis of the forging stress-strain field

Figure 18 shows a semi-cross-sectional view of the simulated equivalent stress-strain contour plots for a wheel hub forging. Figures 18(a) and (b) depict the equivalent stress plots for pre-forging and final forging, respectively, while Figures 18(c) and (d) show the equivalent strain plots for pre-forging and final forging, respectively. Equivalent stress reflects the degree of force exerted on the material during deformation, while equivalent strain reflects the degree of plastic deformation. During the pre-forging stage, the equivalent stress is primarily concentrated in the contact edge region between the billet and the die. The material flows gently only along the pre-forging die cavity, with relatively small differences in deformation resistance and a relatively uniform distribution. Pre-forging only completes the preliminary distribution of the material volume; the amount of plastic deformation is small, the material does not undergo drastic morphological changes, and the strain is low and uniform. During the final forging stage, the material must fill complex cavities and flow toward detailed forming areas such as the wheel spokes. Flow resistance varies across different regions, resulting in differences in the distribution of deformation resistance. Final forging requires filling complex cavities; material in detailed areas such as the wheel spokes must undergo significant plastic flow to complete filling, resulting in a marked increase in local deformation (strain). In contrast, material in the base areas undergoes minimal deformation, with relatively low strain that closely matches the geometric contour of the final forging—high strain in the spoke regions and lower strain in the rim regions.

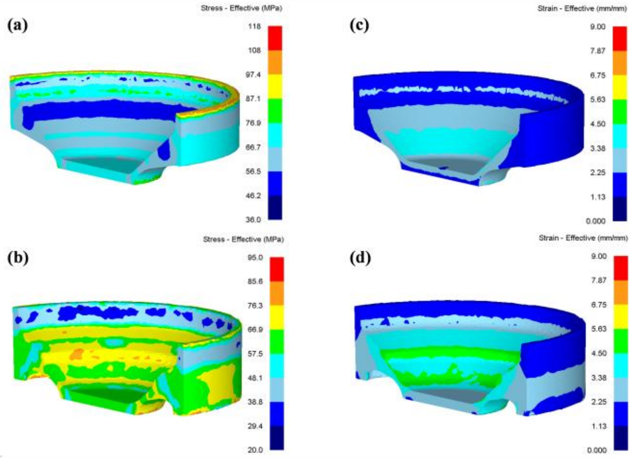

Fig.18 Distribution of equivalent stress and strain during the forming procedure: (a)equivalent stress during pre-forging, (b)equivalent stress during final forging, (c)equivalent strain during pre-forging, (d)equivalent strain during final forging

5.4 Comparative analysis of forging loads

Figure 19 shows the changes in forging load before and after hub optimization. It is evident that the trends in forging load before and after optimization are identical, divided into three stages: die contact, initial deformation, and cavity filling. In all three stages, the load trends are upward, but the rates of increase differ. During the die contact stage, the forging blank begins to contact and initially conform to the die cavity, and the blank begins to undergo slight upsetting; the forging load rises slowly. At the initial deformation stage, the blank starts to exhibit plastic flow under the constraint of the forging die, and its geometry gradually approaches that of the final forged component. With increasing deformation extent, the forging load increases noticeably, and its growth rate accelerates significantly. During the die cavity filling stage, the blank plastically flows into the complex regions of the die cavity to achieve full forming of the target shape. As material flow is gradually confined, deformation resistance rises sharply, which leads to a rapid surge in forging load until it finally reaches its maximum value.

During pre-forging, the maximum forging load reaches 97.5 MN before optimization and declines to 75.6 MN after optimization. In final forging, the peak forging load stands at 76.9 MN in the original process and reduces to 66.7 MN in the optimized process. Following parameter optimization, the maximum forging loads in pre-forging and final forging decrease by 22.46% and 13.26%, respectively. This indicates that the optimized scheme is more effective in reducing peak forging loads, thereby protecting the equipment and improving the quality of the forgings.

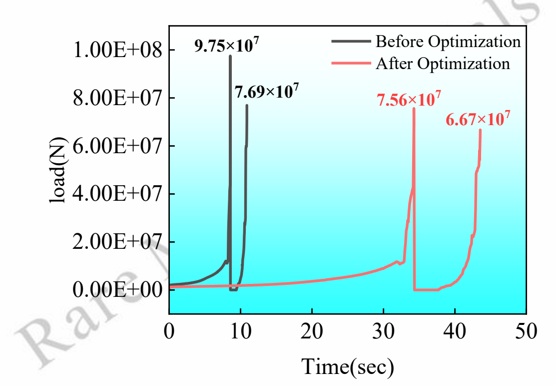

Fig.19 Changes in forging loads before and after optimization

5.5 Comparative analysis of forging damage

Controlling damage to forgings can effectively reduce the risk of cracking and forming defects. Figure 20 shows a comparison of damage contour maps for the wheel hub forging before and after optimization. As shown in the figure, the areas with the highest damage in the wheel hub are still located at the rim edges; the higher the damage value, the greater the corresponding tensile stress, making it more likely for cracks to form during the actual forging process. However, the damage area and values before optimization are significantly higher than those after optimization, demonstrating a marked improvement. After optimization, the original high-damage orange region at the upper edge of the rim has noticeably shrunk, and the overall damage values have decreased. The original yellow regions also show a trend toward transitioning into low-damage green regions, indicating that the material deformation process has become more uniform. This alleviates local stress concentration, results in a more stable load distribution, and effectively improves the quality of forming for the forged component.

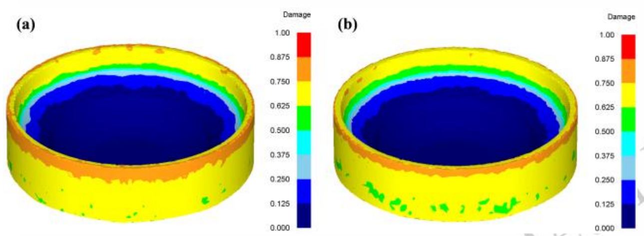

Fig.20 Comparison of damage contour maps for the wheel hub forging before (a) and after (b) optimization.

6 Precision Hot Forging Experiments

6.1 Forging experiment

From the analysis of numerical simulation outcomes, subsequent to the two core forming procedures of pre-forging and final forging, the wheel hub forging exhibits good overall plastic deformation and sufficient forming, with the distribution of relevant field quantities being reasonable and consistent with process expectations. Combining the simulation results with actual forging conditions, hot forging experiments were conducted on a 120MN multi-directional die-forging press, the relevant equipment is shown in Figure 21.

The experimental procedure for wheel hub forging primarily consists of the following steps: First, the billet is placed into a box-type resistance furnace to undergo preheating, and then conveyed to the preheated forging die. To reduce sticking and protect the die, graphite lubricant is sprayed onto the preheated die. Next, the die is closed, and the upper die presses down on the blank; forging is completed when the upper die reaches its preset position. Finally, the upper die is raised to open the mold, and the ejector mechanism on the lower die side is activated to eject the formed wheel hub forging from the cavity. The formed forging is illustrated in Figure 21(f). The geometrical specifications of the experimentally formed wheel hub forging are highly consistent with those of the simulated model. The forged workpiece presents excellent quality accompanied by a smooth surface, and no defects such as insufficient filling or cracking were observed.

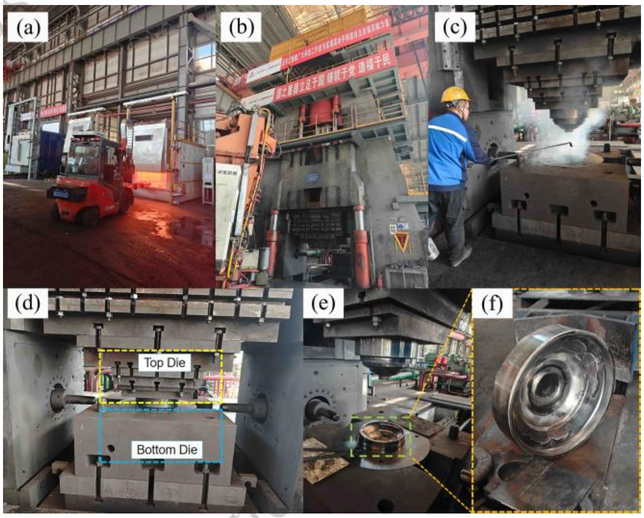

Fig.21 Experiments on the forging of 7050 aluminum alloy wheels: (a) preheating of the billet, (b) forging press, (c)lubrication, (d)forging die, (e)die opening, (f) forged part

6.2 Performance analysis of the forging

Based on the wheel hub forging experiments, it can be concluded that the macroscopic forming quality of the forging is good. To verify that the forged wheel hub meets the service requirements, mechanical property tests were carried out on the forging. Figure 22 displays the tensile testing machine and the tensile specimens used in the experiments. An MTS tensile testing apparatus is utilized to measure and assess the yield strength, tensile strength, elongation after fracture, and reduction in area of the forged part. A summary of the mechanical property test results is provided in Table 6. Every mechanical property of the forged component meets the design requirements, with a particularly marked improvement in yield strength observed. The enhanced yield strength enables the wheel hub to bear higher service stresses, thus better satisfying the demands for service safety and structural durability.

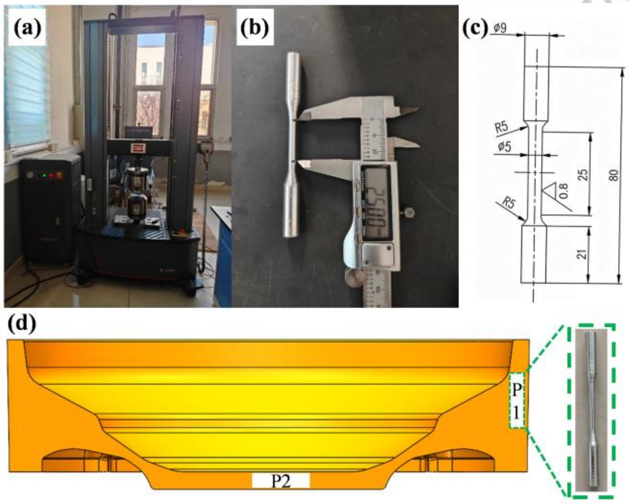

Fig.22 Tensile test of aluminum alloy wheels: (a) MTS tensile testing machine, (b) tensile test specimen, (c) schematic of tensile specimen dimensions, (d)sampling location.

Table 6 Test results for the mechanical properties of forgings

Mechanical properties	Standard requirement	Sample 1	Sample 2	Mean ± SD
Tensile strength/MPa	≥560	578	578	578±0.00
Yield strength/MPa	≥480	512	524	518±8.49
Elongation after fracture/%	≥6	6.0	7.5	6.75±1.06
Reduction in area/%	—	11	12	11.5±0.71

Hardness serves as a key evaluation index for the forming quality of aluminum alloy wheel hub forgings. In this study, Vickers hardness measurements were performed on different locations of the forged part, with the specific test positions shown in Figure 23. All hardness tests were conducted in strict accordance with the GB/T 4340.1-2024 specification. Prior to testing, each specimen was prepared by grinding and polishing. During measurement, a test load of 500gf was applied for a dwell time of 13 seconds. The diagonal lengths of the indentations formed on the sample surface were observed and measured using an optical microscope, and the Vickers hardness values were calculated accordingly. To ensure the accuracy and repeatability of the test results, five independent measurement points were taken for each specimen, and the average value was used as the final hardness result. As detailed in Table 7, the experimental findings demonstrate that the hardness of the forged component is significantly greater than that of the as-received blank.

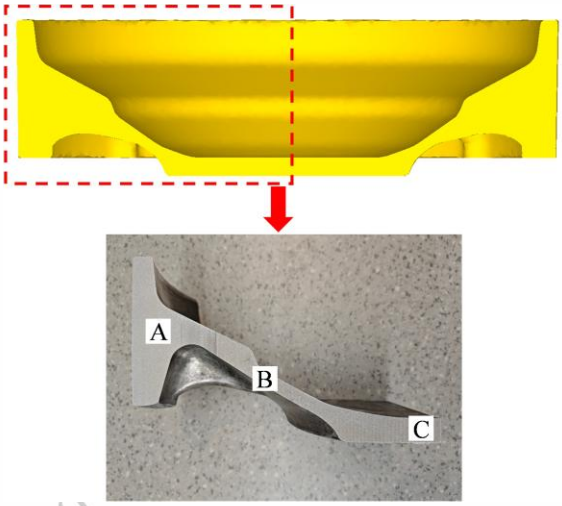

Fig.23 Schematic of sampling points for vickers hardness testing

Table 7 Vickers hardness measurement data

Position	1-HV	2-HV	3-HV	4-HV	5-HV	Mean ± SD
Billet	169.34	170.71	171.85	171.4	168.96	170.45±1.26
Forging A	192.57	189.85	194.59	191.86	191.83	192.14±1.70
Forging B	192.5	195.47	190.91	188.85	192.37	192.02±2.43
Forging C	192.81	188.57	193.03	191.91	193.51	191.97±1.99

To comprehensively evaluate the forming quality of aluminum alloy wheel hub forgings, their microstructures are examined and analyzed. Samples are taken from three typical deformation zones—A, B, and C—shown in Figure 23. After pre-treatment involving mechanical grinding and polishing as well as electrolytic polishing, the samples are characterized using electron backscatter diffraction (EBSD) technology. Figure 24 displays the obtained test results.

The IPF maps indicate that dynamic recrystallization occurs to varying degrees at each sampling location in the forging. After hot forging, the grain structure is greatly refined, accompanied by the formation of a large number of fine grains. Grain size distribution maps further confirm that the grain refinement effect after forming is quite significant, with grains smaller than 20 μm accounting for the dominant proportion in the microstructure. Nevertheless, a small number of coarse deformed grains that failed to complete recrystallization can still be observed in local regions. KAM maps illustrate that the grain interiors mainly correspond to blue areas with low KAM values, whereas regions with high strain and high dislocation density are primarily distributed near grain boundaries. The overall KAM values are relatively low and exhibit good homogeneity, suggesting that an obvious dynamic softening behavior occurs during hot forging. In grain boundary maps, the forged microstructure shows a mixed presence of low-angle and high-angle grain boundaries, among which high-angle boundaries (misorientation > 15°) are predominant. These results further verify that dynamic recrystallization acts as the primary softening mechanism during the hot deformation of the wheel hub forging. By comparison, Region C presents the worst microstructural homogeneity. Combined with the equivalent strain field obtained from Deform-3D numerical simulation, it can be found that the equivalent strain levels in Region C are relatively low. Since the degree of deformation is a key factor in regulating the dynamic recrystallization process, the lower deformation leads to an uneven dynamic recrystallization process in this region, resulting in a distinct mixed grain structure. The grain size distribution range widens to 80 μm, and the proportion of large grains increases significantly. The experimental findings are in excellent agreement with the observed trends in the numerical simulations, confirming the accuracy and dependability of the simulation model.

The optimized hot forging process helps to improve the deformation uniformity of the forging. Appropriate forging temperature and low forging speed can provide sufficient thermal activation conditions and action time for dislocation motion and grain boundary migration, promoting the full progress of dynamic recovery and dynamic recrystallization. A large number of fine equiaxed grains are generated during dynamic recrystallization, achieving significant grain refinement and microstructure homogenization. The above dynamic softening mechanism can effectively alleviate local strain concentration during deformation, inhibit microcrack initiation and damage accumulation, and reduce the overall damage level of the forging. Grain refinement improves the tensile strength of the alloy on the one hand by increasing grain boundary density to hinder dislocation slip; on the other hand, it can coordinate plastic deformation of multiple grains, avoid local stress concentration, and simultaneously increase elongation, which is an important reason for the improvement of the comprehensive mechanical properties of forgings.

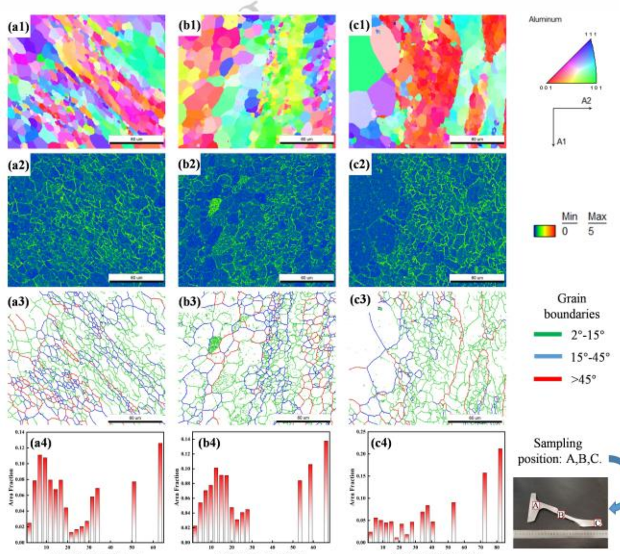

Fig.24 EBSD characterization: (a1, b1, c1) IPF maps, (a2, b2, c2) KAM maps, (a3, b3, c3) grain boundary maps, (a4, b4, c4) grain size distribution maps.

7 Conclusions

1) The high-temperature deformation law of 7050 aluminum alloy is clarified, and a strain-compensated constitutive equation with good accuracy is established. Based on the hot processing map, the optimal hot processing range of the material is determined as deformation temperature of 400–450 °C and strain rate of 0.01–0.1 s^{-1}, which can provide a theoretical basis for the process design of wheel hub forging.

2) A two-stage forming scheme of pre-forging and final forging is adopted combined with the structural characteristics of the wheel hub. The optimal forging process parameters are obtained through response surface methodology: initial forging temperature of 450 °C, forging speed of 5 mm/s, and friction coefficient of 0.216. After optimization, the maximum damage area of the forging is significantly reduced, and the overall damage level shows a downward trend. The peak loads of pre-forging and final forging processes are reduced by 22.46% and 13.26% respectively, and the forming quality and metal flow line distribution of the forging are favorable.

3) The wheel hub forming test results are in good agreement with the numerical simulation predictions. The overall forming quality of the forging is excellent, and all mechanical property indexes meet the production technical requirements. Obvious dynamic recrystallization occurs inside the forging, and the grains are significantly refined, which verifies the effectiveness and reliability of the optimized process scheme proposed in this paper.

References

1 Shen J L, Zhang Q, Tian S S. *Journal of Cleaner Production*[J], 2025, 513: 145677

2 Wang B Z, Zhang Z Y, Xu G C *et al*. Resources, Conservation and Recycling[J], 2023, 191: 106877
3 Dong G J, Li S H, Ma S Z *et al*. Journal of Materials Research and Technology[J], 2023, 24: 3118-3132
4 Yang H J, Qin F C, Cui Y X *et al*. Materials Science and Engineering: A[J], 2026, 959: 150021
5 Chu Q Q, Hou X Y, Cheng Y *et al*. Rare Metal Materials and Engineering[J], 2025, 54(8): 1917-1925
6 Wang S H, Li Z Y, Ma X Y *et al*. Journal of Materials Research and Technology[J], 2025, 35: 3956-3967
7 Hu H, Zhao F, Zhang Z H *et al*. Journal of Manufacturing Processes[J], 2025, 153: 406-420
8 He H L, Chen H Y, Tang M Z *et al*. Journal of Materials Research and Technology[J], 2026, 40: 3521-3539
9 Hu Y H, Zhang D W, Tian C *et al*. Rare Metal Materials and Engineering[J], 2025, 54(6): 1462-1466
10 Yin J, Hu R F, Shu X D. Journal of Materials Research and Technology[J], 2021, 10: 1339-1347
11 Li C L, Li S B, Li X C *et al*. Rare Metal Materials and Engineering[J], 2025, 54(6): 1435-1444
12 Qian D S, Pan Y. Computational Materials Science[J], 2013, 70: 24-36
13 Chen Y, Zhao J F, Kong L *et al*. Results in Engineering[J], 2025, 27: 106108
14 Deb S, Abhilash M B, Immanuel R J *et al*. International Journal of Lightweight Materials and Manufacture[J], 2023, 6 (3): 434-449
15 Dong W Z, Zhao A Y, Wang Z H *et al*. Journal of Manufacturing Processes[J], 2025, 145: 22-33
16 Chamanfar A, Valberg H S, Templin B *et al*. Materialia[J], 2019, 6: 100319
17 Fu Y H, Zhang M B, Chen X *et al*. Journal of Materials Research and Technology[J], 2024, 30: 5056-5068
18 Ge J Y, Shi S X, Zhan X D *et al*. Materials Science and Engineering: A[J], 2024, 911: 146857
19 Li X, Huang C W, Yang J *et al*. Materials Science and Engineering: A[J], 2024, 909: 146824
20 Zhu P, Yang S, Gao Z J *et al*. Journal of Materials Research and Technology[J], 2024, 29: 5271-5281
21 Zhang X Y, Yang Y H, Zheng A L *et al*. International Journal of Refractory Metals and Hard Materials[J], 2026, 135: 107522
22 Kim Y, Jeong H Y, Park J H *et al*. Journal of Materials Research and Technology[J], 2023, 27: 8228-8243
23 Deng W, Wang Z A, He G H *et al*. Materials Today Communications[J], 2025, 42: 111296
24 Łukaszek-sołek A, Krawczyk J, Śleboda T *et al*. Journal of Materials Research and Technology[J], 2019, 8 (3): 3281-3290
25 Obiko J, Mxolisi B, Malatji N. Engineering Reports[J], 2025, 7 (8): e70339
26 Huang X M, Zang Y, Ji H C *et al*. Journal of Materials Research and Technology[J], 2022, 19: 1242-1259
27 Ma L, Wei Z W, Zhou J *et al*. Rare Metal Materials and Engineering[J], 2024, 53(5): 1262-1267
28 Li Y Z, Dong C, Jiang C *et al*. Engineering Failure Analysis[J], 2025, 167: 108994
29 Wu H, Wang M T, Bian G X *et al*. Engineering Failure Analysis[J], 2025, 167: 109054
30 Li C M, Luo H J, Zhao N *et al*. Rare Metal Materials and Engineering[J], 2025, 54(9): 2189-2198

基于仿真与实验耦合的高强铝合金轮毂精密热锻工艺优化

郭贵星[1]，黄晓敏[1,2]，孙富[3]，吴伟奇[3]，毛其林[3]，纪宏超[1,2]

(1. 华北理工大学 机械工程学院，河北 唐山 063210)

(2. 华北理工大学 燕赵钢铁实验室，河北 唐山 063210)

(3. 中冶重工（唐山）有限公司，河北 唐山 063035)

摘　要：针对传统铸造轮毂易产生成形缺陷以及现代车辆对节能减排的高需求，设计了两阶段精密热锻成形工艺用于制备高强轻量化7050铝合金轮毂。通过等温热压缩试验探究7050铝合金锻材的热变形行为，基于Deform-3D软件建立预锻、终锻有限元分析模型，对热锻成形过程开展数值模拟，分析各物理场的分布特征。采用响应面法构建二阶回归模型，以降低锻造载荷、减小锻件损伤为多目标，对工件始锻温度、模锻速度及摩擦系数等关键工艺参数进行优化。优化结果表明，预锻和终锻峰值载荷分别降低了22.46%和13.26%，锻件最大损伤区域明显缩减，整体损伤水平显著降低。依据最优工艺参数进行锻造成形试验，锻件成形质量优良，综合性能均符合生产

技术要求。

关键词：7050铝合金; 轮毂; 热变形行为; 数值模拟; 响应面优化

作者简介：郭贵星，男，2000 年生，硕士研究生，华北理工大学机械工程学院，河北 唐山 063210，电话：0086-315-8805446，E-mail: 18937794971@163.com